



# Cell encapsulation modes in a flow-focusing microchannel: effects of shell fluid viscosity

Mohammad Nooranidoost<sup>1</sup> · Majid Haghshenas<sup>1</sup> · Metin Muradoglu<sup>2</sup> · Ranganathan Kumar<sup>1</sup> 

Received: 24 September 2018 / Accepted: 22 January 2019 / Published online: 5 February 2019  
© Springer-Verlag GmbH Germany, part of Springer Nature 2019

## Abstract

Flow-focusing microencapsulation is an important process to protect the cells in biomedical applications. This article characterizes different cell encapsulation modes and presents the droplet volume distribution, frequency of encapsulation and cell population in terms of inner and outer fluid capillary ratios and viscosity of the shell fluid. The desired mode of at least one cell in a droplet is determined for different capillary number ranges and each viscosity ratios. The droplet volume and frequency of droplet generation are normalized for a combined non-dimensional parameter to classify different patterns of compound droplet formation which helps us to improve single-cell encapsulation process. With increase in orifice radius, the droplet volume increases, and the success rate of cell encapsulation increases. Above a critical radius, the encapsulation mode transitions from one cell to multiple cells captured inside the droplet.

**Keywords** Two-phase flow · Front-tracking method · Flow-focusing · Microfluidics

## 1 Introduction

Cell microencapsulation is a technique used as a delivery system for therapeutic drugs to protect the cells in a safe environment. A typical application of microencapsulation is in bio-printing systems for generating tissue constructs, where the size, shape and the number of microcapsules as well the viability of cells need to be known (Migliarese et al. 2014). Cell microencapsulation has also been used to improve the detection of protein expression (Huebner et al. 2007), antibodies (Love et al. 2006), enzymes (Liu et al. 2009) and cytometry (Edd et al. 2008). Food industry has also taken advantage of this technology by encapsulating live probiotic bacteria cells for processing dairy products (Anal and Singh 2007). In microencapsulation technique, the core substance (cell) needs to be encapsulated with another substance (shell), protecting it from the ambient fluid. This

shell avoids chemical deterioration and minimize any damages of the core substance (Murua et al. 2008).

To encapsulate cells, active (e.g., electrostatic) and passive (e.g., flow focusing) techniques have been used (Collins et al. 2015). Collins et al. (2015) reviewed different methods and their efficiency of cell encapsulation. Most cell encapsulation methods have used passive methods, where droplets are formed hydrodynamically at high throughput by pumping fluids preperpendicularly to the oncoming cells (Edd et al. 2008). Recently, new techniques have also been developed to actively encapsulate cells, which have the potential to control droplet formation and improve the efficiency of single-cell encapsulation (Collins et al. 2013). In active techniques, external forces such as electrical forces are applied to emulsion that could provide better control on the encapsulation process, however, have limitations (Collins et al. 2015; Castillo-Orozco et al. 2017; Wilson et al. 2013). For example, high electrode voltage may damage cells and cause them to lose cell activity and viability. On the other hand, passive techniques such as flow focusing has the advantages of simplicity and high throughput of droplets in kHz, but has less control over droplet formation (Edd et al. 2008). In this study, flow-focusing technique is used to generate compound droplets.

In terms of emerging studies in microchannels, glass capillary tubes and polydimethylsiloxane (PDMS) have

✉ Ranganathan Kumar  
ranganathan.kumar@ucf.edu

<sup>1</sup> Department of Mechanical, Materials and Aerospace Engineering, University of Central Florida, Orlando, FL 32816, USA

<sup>2</sup> Department of Mechanical Engineering, Koç University, Rumelifeneri Yolu, Sariyer, 34450 Istanbul, Turkey

produced single (Anna et al. 2003; Wehking et al. 2013; Liu and Zhang 2009; Nie et al. 2008; Gupta et al. 2016) or double emulsion (Utada et al. 2005; Vladisavljević et al. 2012; Lao et al. 2009). Such droplet formation in microfluidic systems has been possible through coflowing (Chen et al. 2013; Zhao 2013), T junction (Glawdel et al. 2012; Tan and Nguyen 2011; Carrier et al. 2014; Xu et al. 2008) and flow-focusing (Tan and Nguyen 2011; Nooraidoost et al. 2016; Abate et al. 2011; Cruz-Mazo et al. 2016; Derzsi et al. 2013) devices. Due to the large surface-to-volume ratio, the role of surface tension becomes important, as are the flow rates of the continuous and dispersed droplet phases, and the geometry of the channel. The encapsulation device works hydrodynamically by pumping different ingredients (i.e., inner fluid and cells) through inner channels and are enclosed in a larger microchannel containing a fluid (i.e., outer fluid) forming the outer core of the encapsulating shell. Due to the symmetric design of flow-focusing geometries, the continuous fluid employs shearing force symmetrically from outer subchannel, which enables more stable and controllable formation of droplets (Zhao 2013). Dynamics of double emulsions have also been investigated in these devices experimentally (Utada et al. 2005; Vladisavljević et al. 2012; Zhao 2013; Chong et al. 2015). Utada et al. (2005) fabricated a coaxial microcapillary flow-focusing device to generate double emulsions in a single step with precisely controlled numbers of core droplets per shell droplet and adjustable droplet size. Later, researchers conducted multiple emulsion formation with various combination of fluids in these coaxial flow-focusing devices to control flow dynamics by adjusting effective parameters (Chu et al. 2007; Che et al. 2017; Seo et al. 2007). These studies show that fluid properties, flow rate and the geometry of the microchannel are the main parameters to characterize droplet formation.

Droplet-based microfluidics is proven to be important in encapsulating living cells by forming compound droplets (shell/cell) at very high throughput. Flow-focusing devices have great potential to control flow dynamics and produce these compound droplets downstream of the channel. In this technique, hydrogels are mainly used as a shell fluid to encapsulate different types of cells, providing a three dimensional environment similar to that experienced in vivo and, therefore, producing tissues similar to those found in the body (Hunt and Grover 2010; Akbari and Pirbodaghi 2014). Recently, researchers performed experiments to statistically study this encapsulation method. Their study shows that initial random distribution of cells at the inlet follows a Poisson distribution for numbers of cells per droplet (Moon et al. 2011). They found that evenly spaced (Edd et al. 2008) and close-packed (Abate et al. 2009) ordering of the cells within the channel can improve the probability of single-cell encapsulation. Edd et al. (2008) encapsulated high density suspension of cells

with a method that causes cells to self-organize into evenly spaced streams at high capillary numbers, overcoming the intrinsic limitations set by Poisson statistics and ensuring that every drop contains a cell. They used a cross junction microfluidic device with a rectangular high aspect ratio cross section. At moderate Reynolds numbers, due to inertial forces, particles focus to two equilibrium positions centered at the long face of the channel (Di Carlo 2009). This ordering of cells can improve the efficiency of cell encapsulation process. Other techniques that actively order cells and focus the particles on centerline include acoustic focusing which can be achieved by matching the acoustic particles of the dispersed and continuous phases (Fornell et al. 2018).

The production of compound droplets and cell encapsulation in flow-focusing devices have been mainly studied experimentally. Numerical study can not only guide the experiments for new fluids, but also predict the success rate and modes of encapsulation. A few numerical studies can be found in compound droplet formation in flow-focusing configurations (Zhou et al. 2006; Homma et al. 2014; Chen et al. 2015; Nabavi et al. 2015). Compound droplet formation was simulated in a coaxial dual nozzle flow-focusing configuration and a phase diagram was developed (Zhou et al. 2006; Homma et al. 2014). A double emulsion droplet formation was numerically investigated by the Volume of Fluid (VOF) method (Chen et al. 2015). Double emulsion production in a three-phase glass capillary device was numerically studied (Nabavi et al. 2015) using the VOF continuum surface force (VOF-CSF) model, that predicted the change in droplet size by adjusting the flow rate ratio.

To the best of our knowledge, all the existing numerical studies on compound droplet generation in a flow-focusing configuration have used a coaxial dual nozzle configuration to produce compound droplets from three inlet flows. In addition, there has been no work in the encapsulation of predefined cells. Following Nooraidoost et al. (2017), this current study numerically investigates the generation of compound droplets (cell/shell) in an axisymmetric flow-focusing device. We characterize different modes of cell encapsulation by modifying the fluid and flow properties, and the geometry of the device to study the drop size distribution and cell population in the capsule. The numerical method is based on a three-phase finite-difference/front-tracking algorithm developed by Tryggvason et al. (2001). Extensive simulations are performed to investigate the compound droplet formation for various flow rates of the inner and outer fluid, viscosity of inner fluid and the geometry of the flow-focusing device. The choice of the fluids is made such that Newtonian fluid assumption is applicable for the viscosity ratios (inner to outer fluid) of 0.5, 1 and 2.

## 2 Formulation and numerical method

Several numerical methods such as Volume of Fluid (VOF) (Hirt and Nichols 1981), Level Set (LS) (Osher and Sethian 1988), front-tracking (Unverdi and Tryggvason 1992) and coupled VOF/LS (Haghshenas et al. 2017) have been developed for the simulation of interfacial flows. In this research, an axisymmetric front-tracking method is utilized and is previously validated for droplet formation of a two-phase microfluidic system (Noorandooost et al. 2016). The governing equations are briefly described here in the framework of the finite-difference/front-tracking method (Tryggvason et al. 2001). The front-tracking method is proven to be a viable tool for simulation of interfacial flow in microchannels (Noorandooost et al. 2016; Homma et al. 2014; Izbassarov and Muradoglu 2016) and biological systems (Tasoglu et al. 2010). Following Tryggvason et al. (2001) a one-field formulation is used in which a single set of governing equations is solved in the whole flow field with different material properties in each phase. The flow is assumed to be incompressible and the material properties are constant in each phase. In this formulation, the continuity and momentum equations can be written as

$$\nabla \cdot \mathbf{u} = 0, \quad (1)$$

$$\frac{\partial \rho \mathbf{u}}{\partial t} + \nabla \cdot (\rho \mathbf{u} \mathbf{u}) = -\nabla p + \nabla \cdot \mu (\nabla \mathbf{u} + \nabla \mathbf{u}^T) + \int_A \gamma \kappa \mathbf{n} \delta(\mathbf{x} - \mathbf{x}_f) dA, \quad (2)$$

where  $\mu$ ,  $\rho$ ,  $p$  and  $\mathbf{u}$  denote the viscosity, density, pressure and velocity vector, respectively. The effects of surface tension are fully accounted through the body forces distributed near the interface which is represented in the last term in Eq. (2). In this term,  $\gamma$  is the surface tension coefficient,  $\kappa$  is the interface curvature, and  $\mathbf{n}$  is the unit vector normal to the interface. The surface tension acts only on the interface as indicated by the delta function,  $\delta$ , whose arguments  $\mathbf{x}$  and  $\mathbf{x}_f$  are the points at which the equation is being evaluated and a point at the interface, respectively. It is also assumed that the material properties remain constant following a fluid particle. The density and viscosity vary discontinuously across the fluid interface and are given by

$$\rho = \begin{cases} \rho_i \phi + \rho_o(1 - \phi) & \text{if } \phi \leq 1 \\ \rho_c(\phi - 1) + \rho_i(2 - \phi) & \text{otherwise,} \end{cases} \quad (3)$$

$$\mu = \begin{cases} \mu_i \phi + \mu_o(1 - \phi) & \text{if } \phi \leq 1 \\ \mu_c(\phi - 1) + \mu_i(2 - \phi) & \text{otherwise,} \end{cases}$$

where the subscripts c, i and o denote the properties of cell, inner fluid and outer fluid, respectively. In Eq. (3),  $\phi$  is the indicator function computed at every time step to distinguish each fluid and it is defined as

$$\phi = \begin{cases} 2 & \text{in cell,} \\ 1 & \text{in inner fluid,} \\ 0 & \text{in outer fluid.} \end{cases} \quad (4)$$

The governing equations (1 and 2) are solved on a staggered Cartesian Eulerian grid using a projection method, while the interfaces between the fluids are explicitly tracked by a separate Lagrangian grid, consisting of marker points connected by front elements. The Lagrangian grid is reconstructed at each time step by splitting/deleting very large/very short front elements to keep the front element size nearly uniform and comparable to the Eulerian grid size. The surface tension is computed on this Lagrangian grid and is projected on Eulerian grid points to be added to the Navier–Stokes equation. The spatial derivatives are approximated using a central difference method and the time integration is done using a simple first order scheme. A complete description of the front-tracking method can be found in the work of Unverdi and Tryggvason (1992) and Tryggvason et al. (2001).

## 3 Problem statement

The flow-focusing geometry consists of a main cylindrical microchannel (outer pipe) and a concentric subchannel (inner pipe) at the entrance (Fig. 1). The flow is assumed to be incompressible and axisymmetric. Therefore, only one half is used as the computational domain. Inner and outer fluids enter the flow-focusing configuration from the inner pipe and the annular pipe, respectively. The interface between the inner and the outer fluid is initially flat at the exit of the inner pipe. The flow is initiated instantaneously by imposing fully developed profiles in the inner pipe and the annular tube, the pressure is kept constant at the outlet,

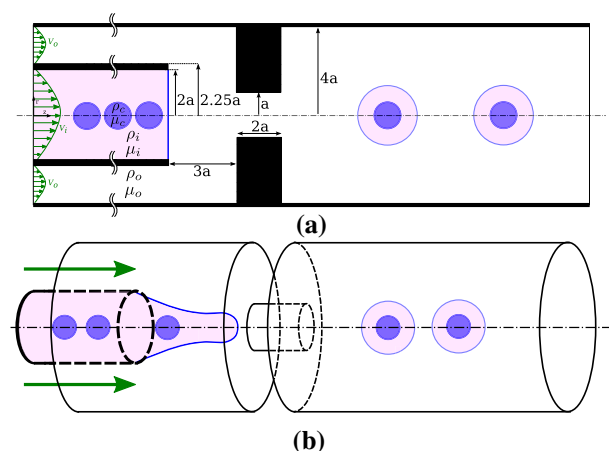


**Fig. 1** a 2D and b 3D Schematic illustration of the flow-focusing geometry

and no-slip boundary condition is used at the wall of the tube. We place twenty cells within the inner subchannel. The cells are modeled as deformable spherical particles with uniform size and constant surface tension. The cells are initially evenly spaced (the distance between the cells is 10  $\mu\text{m}$ ) to improve the efficiency of single-cell encapsulation. In general, it is difficult to align the cells at the axis (Di Carlo 2009) in a circular cross section, however, within the orifice the inner flow converges to a diameter equivalent to the cell size, leading and focusing the cells to the axis.

A uniform Cartesian grid is employed, and a grid convergence study is done to determine the minimum grid size required to reduce the spatial discretization error below a threshold value. It is found that a computational grid containing  $128 \times 1280$  cells in the radial and axial directions, respectively, is sufficient to reduce the spatial error below 2% for all flow configurations. Therefore, this grid resolution is used in all the results presented in this paper unless specified otherwise.

The governing equations (1 and 2) are solved in their dimensional forms but the results are expressed in terms of relevant non-dimensional quantities. Note that the reference length scale in this study is the radius of the orifice ( $a = 20 \mu\text{m}$ ). The geometry of the flow-focusing configuration is fixed in all the results except, where we study the effects of geometry on droplet size. The non-dimensional numbers used to develop a flow regime map are the inner and outer capillary numbers,  $Ca_i = \frac{\mu_i \bar{u}_i}{\gamma}$  and  $Ca_o = \frac{\mu_o \bar{u}_o}{\gamma}$ , i.e., viscous to interfacial forces, and viscosity ratio, ( $\beta = \frac{\mu_i}{\mu_o}$ ). Also, inner and outer Weber numbers, i.e., inertial to interfacial force, defined as  $We_i = \frac{\rho \bar{u}_i^2 a}{\gamma}$  and  $We_o = \frac{\rho \bar{u}_o^2 a}{\gamma}$ , respectively.  $\bar{u}_i$  and  $\bar{u}_o$  are the average velocities of the inner and outer fluids at the inlet, respectively. Gravitational effects are negligible in microchannels, and densities of all three fluids are set to be equal. Interfacial tension of shell/cell and outer fluid/shell are set to be the same as  $\gamma = 0.02 \text{ N/m}$  and the viscosity of outer fluid and the cell are fixed as  $\mu_c = \mu_o = 0.002 \text{ N s/m}^2$ . Note that the viscosity of the cell and the interfacial tension of cell/shell interface do not affect the cell encapsulation dynamics significantly, as also seen by Tasoglu et al. (2010). Since the cell needs a favorable shell fluid to sustain itself, different shell viscosities are considered for encapsulation. The simulated fluids have different viscosity ratios ( $\beta = 0.5, 1, 1.5$  and 2) and a wide range of capillary numbers

( $10^{-4} \leq Ca_i \leq 5 \times 10^{-3}$  and  $10^{-4} \leq Ca_o \leq 5 \times 10^{-3}$ ), and Weber numbers  $2 \times 10^{-5} \leq We_i \leq 5 \times 10^{-2}$  and  $2 \times 10^{-5} \leq We_o \leq 5 \times 10^{-2}$ .

## 4 Results and discussion

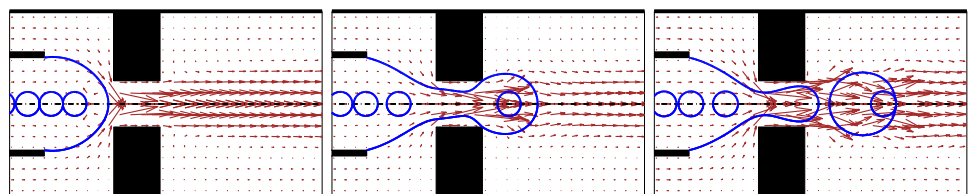
In the encapsulation process (Fig. 2), as the shell fluid begins to penetrate the outer fluid, the cell loads into a forming droplet, which encounters a viscous shear stress induced by the outer fluid. The cross section of the channel gets narrower close to the orifice region and focuses the inner flow to a streamtube of diameter  $\approx 20 \mu\text{m}$  at the orifice. The diameter of this streamtube is similar to the cell size. The outer flow velocity at the orifice is an order of magnitude higher than the average outer flow velocity, typically 20 times as observed in Fig. 2. About 200 simulations have been used to develop the flow regime map in this work. The outer flow velocity at the inlet is in the range 0.001–0.05 m/s. For an outer velocity of 0.05 m/s, the maximum velocity seen at the periphery of the orifice is 1.1 m/s. This velocity is of the same order of magnitude (1.37 m/s) for the experimental case reported in the rectangular geometry (Edd et al. 2008).

In Fig. 2, the droplet thread remains attached to the shell fluid subchannel, while the orifice raises the local pressure around the newly formed droplet. The driving pressure force may overcome the resisting forces of surface tension and viscosity to pinch-off the droplet and complete the formation of a compound droplet. The cell is isolated by the shell and the compound droplet flows downstream the flow.

In this study, multiple flow configurations are studied that generate compound droplets. In particular, the effects of capillary number of both inner and outer fluids ( $Ca_i$  and  $Ca_o$ ), viscosity of the inner fluid ( $\beta$ ) and orifice radius ( $a'$ ) are investigated. A phase diagram of four modes of cell encapsulation will be presented for a range of inner and outer capillary numbers at different viscosity ratios, and the volume and frequency profiles are presented in terms of relevant non-dimensional parameters to understand the most important modes for successful encapsulation for all viscosity ratios.

The cell encapsulation process depends substantially on inertial, viscous and interfacial forces. Thus, the capillary number of the fluids has a significant influence on the flow

**Fig. 2** Time evolution of cell encapsulation process at  $Ca_i = 10^{-3}$ ,  $Ca_o = 10^{-3}$  and viscosity ratio  $\beta = 1$ . Velocity vectors are shown to represent flow dynamics. The snapshots are taken at different times



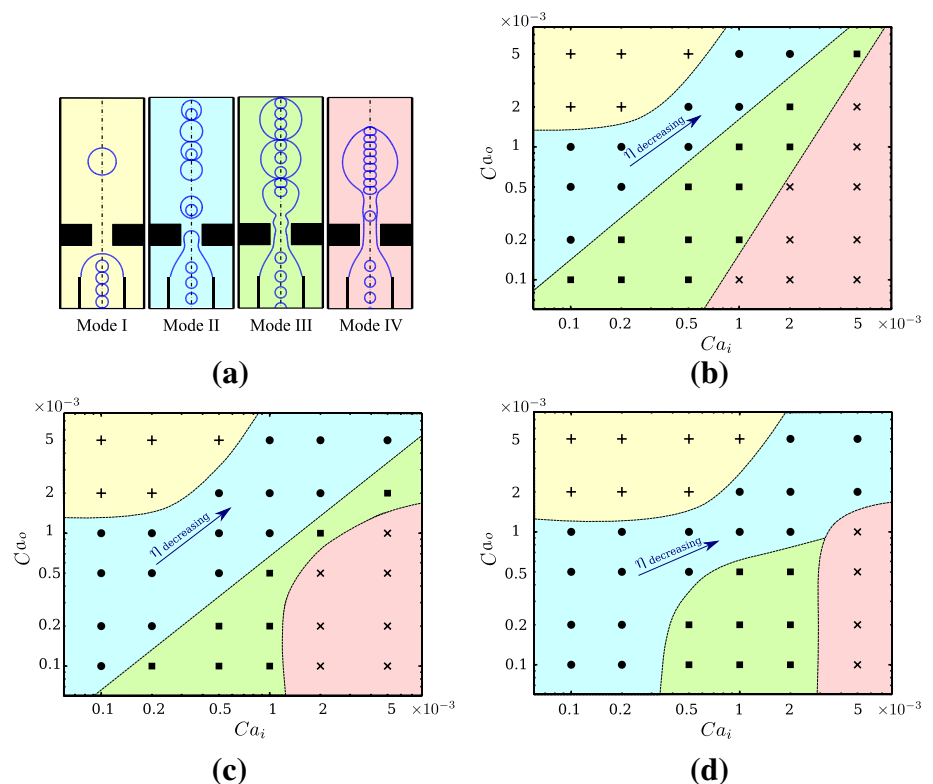


dynamics and the droplet formation process. Simulations have been performed for a wide range of capillary number of both inner and outer phases ( $Ca_i$  and  $Ca_o$ ) at various values of viscosity ratios ( $\beta$ ). Figure 3 shows the phase diagram of successful/unsuccessful cell encapsulation for  $10^{-4} \leq Ca_i \leq 5 \times 10^{-3}$  and  $10^{-4} \leq Ca_o \leq 5 \times 10^{-3}$  at fixed values of  $\beta = 0.5, 1$  and  $2$ . It is found that the successful encapsulation of the cells occurs only within a band on the  $Ca_i$  and  $Ca_o$  plane. Simulations reveal four distinct modes of cell encapsulation (Fig. 3a): mostly empty droplets with no cells inside (Mode I); at most one cell per droplet (Mode II); at least one cell per droplet (Mode III) and no breakup to form cell-encapsulated droplets (Mode IV). In biomedical applications, encapsulated cells occur in mode II and III, with the single-cell per droplet (Mode II) being the most desirable in drug delivery and bio-printing systems (Edd et al. 2008). These different modes are shown in Fig. 3b–d for  $\beta = 0.5, 1$  and  $2$ . The approximated trend lines show the border between different modes. When  $Ca_i$  is much smaller than  $Ca_o$  (i.e.,  $\frac{Ca_i}{Ca_o} \ll \mathcal{O}(1)$ ), high flow rate of the outer fluid prevents the cells from moving fast enough to enter a droplet and as a result, most of the generated droplets are empty (Mode I; yellow patch). Note that the cases with less than 10% of the cell-containing droplets are considered as Mode I. When  $\frac{Ca_i}{Ca_o} \simeq \mathcal{O}(1)$ , the droplet generation is more effective, and the number of cells per droplet depends on  $\frac{Ca_i}{Ca_o}$  and  $\beta$ . At a fixed value of  $\beta$  for relatively lower  $\frac{Ca_i}{Ca_o}$ , droplets contain at

most one cell (Mode II; blue patch), while at higher  $\frac{Ca_i}{Ca_o}$ , the inner flow rate is higher such that the cells have more time to load the forming droplet. Therefore, multiple cells get encapsulated in a larger droplet as the residence time is higher to form such a compound droplet (Mode III; green patch). As  $\frac{Ca_i}{Ca_o}$  increases, the higher inner flow rate and the fast cell migration downstream of the channel prevent pinch-off and encapsulation fails (Mode IV; pink patch). The region in which successful encapsulation occurs varies for different viscosity ratios ( $\beta$ ). As the viscosity of the inner fluid increases, there is more time for the cell to occupy the forming droplet, thus altering the encapsulation mode. By increasing  $\beta$ , successful encapsulation occurs at mid-range  $Ca_o$  (i.e.,  $Ca_o \simeq 10^{-3}$ ) and high  $Ca_i$  and the transition between different modes have a shift toward higher  $Ca_i$  at a fixed  $Ca_o$  (Fig. 4). This means that cell encapsulation mode can be changed to the desired mode (Mode II), by manipulating  $\beta$ . For instance, the cell encapsulation mode can be altered at a fixed  $Ca_i$  and  $Ca_o$  from mode III to mode II by increasing  $\beta$ .

In cell encapsulation technique, having more cell encapsulating droplets indicates a higher success rate ( $\eta$ ), which is defined as the ratio of cell-containing droplets to the total generated droplets. In mode II, the success rate decreases when both  $Ca_i$  and  $Ca_o$  increase (Fig. 3b–d). At relatively low  $Ca_i$  and  $Ca_o$ , necking occurs at a higher time constant to allow the cells sufficient time to occupy the forming droplet

**Fig. 3** **a** Different modes of cell encapsulation. **b** Phase diagram of different modes at  $\beta = 0.5$  **c**  $\beta = 1$  and **d**  $\beta = 2$ . Color patches represent different cell encapsulation modes: yellow: Mode I, mostly empty droplets with no cells inside; blue: Mode II, at most one cell per droplet; green: Mode III, at least one cell per droplet; pink: Mode IV, no breakup to form cell-encapsulated droplets;  $\eta$  = success rate of encapsulation. (Color figure online)



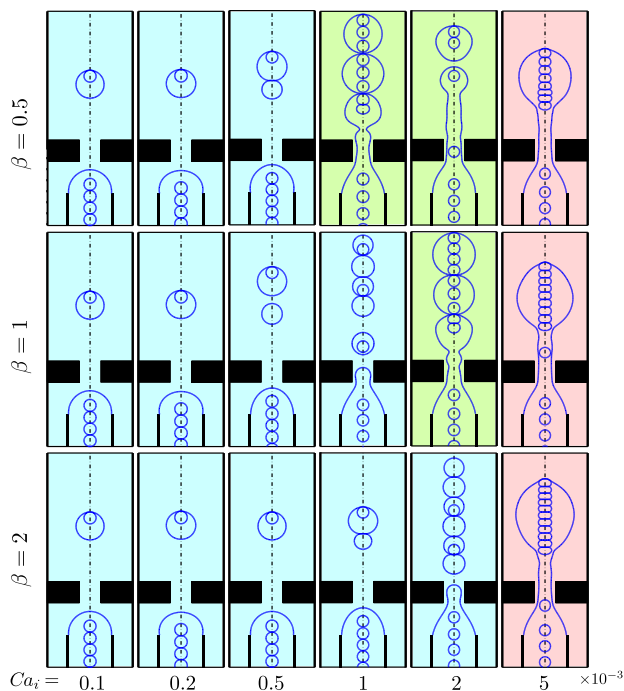


**Fig. 4** Snapshots of cell encapsulation for  $10^{-4} \leq Ca_i \leq 5 \times 10^{-3}$  at  $\beta = 0.5, 1$  and  $2$  for a fixed  $Ca_o = 10^{-3}$ . Color patches represent different cell encapsulation modes: yellow: Mode I, mostly empty droplets with no cells inside; blue: Mode II, at most one cell per droplet; green: Mode III, at least one cell per droplet; pink: Mode IV, no breakup to form cell-encapsulated droplets. (Color figure online)

to reach the maximum success rate of nearly 100%. The configuration of initial evenly spaced cells within the channel results in a high success rate, as is also corroborated by Edd et al.'s (2008) experiment. The encapsulation process is considered a failure when  $\eta \leq 10\%$  (Mode I) at low  $Ca_i$  and high  $Ca_o$ , where the inner and outer flow rates allow droplets to form at a frequency too high compared to cell loading frequency. As a result, the probability of encapsulation is low at these capillary numbers. Note that  $\eta$  is undefined in mode III and IV due to the existence of multiple cells per droplet and failure in encapsulating cells, respectively.

Successful cell encapsulation mainly occurs in the dripping regime, where the pinch-off of the thread takes place close to the orifice. In this regime, cells have more time to occupy the forming droplet which increases the probability of droplets containing cells. Such monodisperse and predictable generation of droplets in the dripping regime is favorable in biomedical applications, and is also advantageous in the cell encapsulation process. However, when the jetting regime arises, where the flow rate of inner fluid is much higher than the flow rate of the outer fluid. A jet is produced in this regime which flows downstream of the flow and droplets pinch-off at the top of the jet with a very high frequency. In this regime, the frequency of droplet generation (DG) is

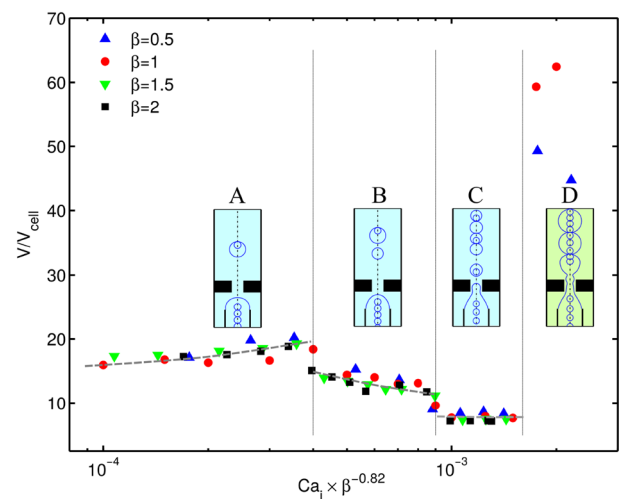


**Fig. 5** Non-dimensional droplet volume for  $10^{-4} \leq Ca_i \leq 5 \times 10^{-3}$  at  $\beta = 0.5, 1, 1.5$  and  $2$  and for a fixed  $Ca_o = 10^{-3}$ . Four different patterns are coded as A, B, C and D. Color patches represent different cell encapsulation modes: blue: Mode II, at most one cell per droplet; green: Mode III, at least one cell per droplet. (Color figure online)

usually much higher than frequency of cell loading (CL), and therefore, most of the droplets do not contain any cells. It is found that for successful single-cell encapsulation,  $\frac{Ca_i}{Ca_o} \approx \mathcal{O}(1)$ . The flow regime shows that it is possible to capture cells at low or high  $Ca_i$  and  $Ca_o$  as long as this ratio is maintained near unity. This is in contrast with rectangular geometry, where  $\frac{Ca_i}{Ca_o}$  can be small to achieve single-cell encapsulation. Edd et al. (2008) achieved single-cell encapsulation for relatively smaller  $\frac{Ca_i}{Ca_o} \approx 0.037$ . This disagreement is possibly due to the different design of the two geometries. For axisymmetric flow-focusing configurations, the outer and inner fluids flow in parallel with the outer flow accelerating significantly at the orifice. In cross junction geometries, the outer fluid flows in at high speed perpendicularly for successful encapsulation.

Droplet volume, generation frequency and droplet size distribution vary for different non-dimensional numbers. A combination of parameters can be found for the normalized average droplet volume of different  $Ca_i$  and  $\beta$  as a function of  $Ca_\beta = Ca_i \times \beta^{-0.82}$  for a given capillary number of the outer fluid at  $Ca_o = 10^{-3}$  (Fig. 5). The droplet dimension is represented by the average volume of the generated droplets, whether those droplets contain cells or not. It is normalized using the initial cell volume ( $V_{cell} = 4.19 \times 10^{-6} \mu\text{L}$ ). Figure 5 clearly classifies the transition of droplet formation patterns into four basic regimes: (A) uniform large droplets with low frequency, where the droplet volume increases linearly with  $Ca_\beta$ ; (B) non-uniform size droplets with low frequency, where the droplet volume decreases on average with  $Ca_\beta$ ; (C) smaller uniform droplets with relatively high frequency, where the droplet volume increases on average with  $Ca_\beta$ ; (D) a transition to higher volumes.

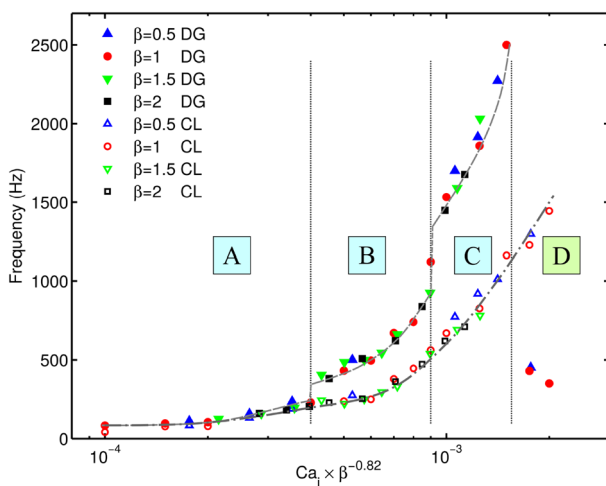
frequency, where pinch-off occurs at the orifice and droplet volume is nearly constant with  $Ca_\beta$ . Here, the minimum droplet size (where the shell thickness is minimum) exists, where at most one cell is present inside the droplet, a condition which is desirable for most biomedical applications. Mode II of cell encapsulation occurs in regions (A, B and C), while mode III appears in region (D), where large droplets appear with unpredictable uniformity. The favorable cell encapsulation (Mode II) occurs for  $Ca_\beta \leq 1.6 \times 10^{-3}$  and the desired droplet formation pattern can be controlled by adjusting  $Ca_\beta$ . At  $Ca_\beta \approx 1.6 \times 10^{-3}$ , a sudden jump in droplet volume occurs, since the frequency of loading cells inside the forming droplet overcomes the frequency of droplet formation. This results in the generation of large droplets with no uniformity.

Figure 6 shows the frequency profiles of droplet generation (DG) and cell loading (CL) with  $Ca_\beta$ . For  $Ca_\beta \leq 1.6 \times 10^{-3}$  in region (A), the frequency of droplet generation is almost equal to frequency of cell loading, with almost all droplets containing cells. In region (B), a secondary droplet with no cells inside forms after each primary pinch-off. Therefore, the droplets are generated with a frequency roughly twice the frequency of cell loading, resulting in 50% drop in cell encapsulation success rate. In region (C), when  $Ca_\beta$  is increased, the frequency of droplet generation increases dramatically and monotonically. This drastic increase in droplet generation frequency which is much higher than the cell loading, resulting in lower success rate of encapsulation. Beyond the critical value of  $Ca_\beta$  ( $\approx 1.6 \times 10^{-3}$ ), the cell encapsulation mode transfers

from mode II to mode III, where the droplets form with a frequency that is lower than the frequency of cell loading.

The cell encapsulation success rate is substantially affected by the inner and outer fluid flow rates. For a fixed outer flow rate, as the inner flow rate increases, cells load faster into the orifice and as a result the cell loading frequency increases. This is shown clearly in Fig. 6. In this figure, for a fixed  $Ca_o = 10 \times 10^{-3}$ , as  $Ca_i$  is increased, droplet generation frequency increases, but the cell loading frequency does not increase at the same rate. The different patterns, A, B and C are all in mode II of single-cell encapsulation. In A, the success rate of encapsulation is high, because the two frequencies are about the same. In B and C, however, the droplet generation frequency is higher as  $Ca_i$  is increased, making the success rate of encapsulation lower. If the outer flow rate is increased, i.e., for higher  $Ca_o$ , the droplet generation frequency would also increase, but without a corresponding increase in cell loading frequency. It is still possible to encapsulate single cells at a reasonably high success rate at high  $Ca_i$  and  $Ca_o$  as shown in Fig. 3. However, as discussed above, the success rate would be lower.

Additional simulations are performed to investigate the effect of orifice geometry on cell encapsulation. To study this geometric effect, we define a non-dimensional orifice radius ( $a^* = \frac{a}{a_0}$ , where  $a$  is the original radius). Figure 7 shows the phase diagram of cell encapsulation for  $10^{-4} \leq Ca_i \leq 5 \times 10^{-3}$  and  $10^{-4} \leq Ca_o \leq 5 \times 10^{-3}$  at fixed values of  $a^* = 0.8, 1$  and  $1.4$ . Viscosity of fluids is kept constant in this geometrical study ( $\beta = 1$ ). It is found that modes II and III of cell encapsulation occur only within a band on the  $Ca_i$  and  $Ca_o$  plane. For  $a^* = 0.8$ , the narrowness of the orifice helps the necking process and as a result, successful single-cell encapsulation occurs for a wide range of  $Ca_i$  and  $Ca_o$ . In general, for the smallest orifice, there is a larger area of the regime map, i.e., a wider range of inner and outer capillary numbers, at which single-cell encapsulation is successful. For  $Ca_o < 0.5 \times 10^{-3}$ , the blue region of mode II extends up to  $Ca_i \approx 1.5 \times 10^{-3}$ , which is not possible for larger orifices,  $a^* = 1$  and  $1.4$ . Beyond  $Ca_o > 10^{-3}$ , mode II occurs at higher  $Ca_i$  as for larger orifices, however, the region narrows at much higher  $Ca_o$ . Since the necking process occurs faster for  $a^* = 0.8$  there is a higher probability of a single cell entering the forming droplet (Mode II), however, due to higher velocity at the orifice, multiple cell encapsulation (Mode III) does not occur, as there is not sufficient time for the forming droplet to encapsulate more than one cell. This gives rise to a larger blue (Mode II) region, no green (Mode III) region and a smaller pink (Mode IV) region compared to the larger orifices of  $a^* = 1.0$  and  $1.4$ . For all geometries, at and beyond  $Ca_o = 10^{-3}$ ,  $Ca_i$  needs to be sufficiently large for



**Fig. 6** Frequency of droplet generation (DG) versus cell loading (CL) for  $10^{-4} \leq Ca_i \leq 5 \times 10^{-3}$  at  $\beta = 0.5, 1$  and  $2$  and for a fixed  $Ca_o = 10^{-3}$ . Four different patterns are coded as A, B, C and D. Color patches represent different cell encapsulation modes: Blue: Mode II, at most one cell per droplet; Green: Mode III, at least one cell per droplet. (Color figure online)

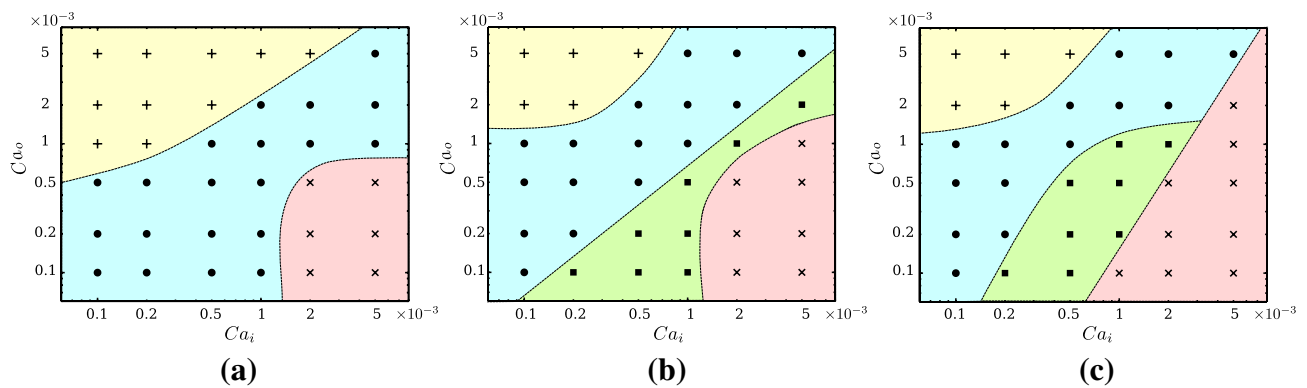


**Fig. 7** Phase diagram of different modes at **a**  $a^* = 0.8$ , **b**  $a^* = 1$  and **c**  $a^* = 1.4$ . Color patches represent different cell encapsulation modes: yellow: Mode I, mostly empty droplets with no cells inside; blue: Mode II, at most one cell per droplet; green: Mode III, at least one

cell per droplet; pink: Mode IV, no breakup to form cell-encapsulated droplets. Viscosity of the fluids is kept fixed ( $\beta = 1$ ). (Color figure online)

successful single-cell encapsulation. This geometrical study reveals that by increasing the radius of the orifice, the inner fluid has more time to pass the contraction region, the pinch-off is postponed and will change the mode of encapsulation. Therefore, different modes of encapsulation appear to shift toward lower  $Ca_i$  and higher  $Ca_o$ . Thus, while it is possible to achieve single-cell encapsulation for a wider range of  $Ca_i$  and  $Ca_o$ , it is better accomplished for a combination of (low  $Ca_i$ –low  $Ca_o$ ) or (high  $Ca_i$ –high  $Ca_o$ ). In other words,  $\frac{Ca_i}{Ca_o} \approx \mathcal{O}(1)$ .

Further simulations are performed to study the effects of orifice radius on droplet size, frequency of cell loading (CL) and frequency of droplet generation (DG) for different radii of orifice at  $Ca_i = 10^{-3}$ ,  $Ca_o = 10^{-3}$  and  $\beta = 1$ . As shown in Fig 8, the orifice radius influences the droplet formation significantly, which may also change the mode of encapsulation. Frequency of cell loading (CL), i.e., the frequency at which the cells enter the orifice region, is highly dependent of how fast they enter the microchannel, and orifice geometry would be unable to manipulate it. Therefore, the frequency of cell loading for a fixed  $Ca_i$  is roughly constant. For devices with small orifice radius, droplets form with high throughput, and cell encapsulation occurs in the blue region (Mode II), where there is utmost one cell per droplet. Here, the frequency of droplet formation is much higher than the frequency of cell loading and as a result, the success rate of cell encapsulation is low.

As the radius of orifice increases, frequency of droplet generation (DG) decreases monotonically, while the frequency of cell loading (CL) remains constant. Above a critical value of non-dimensional orifice radius ( $a^* \approx 1.15$ ), the frequency of cell loading overcomes the frequency of droplet generation, and therefore, cells have more time to occupy the forming droplet. Thus, the mode of cell encapsulation transfers from mode II to mode III, where there are multiple cells per

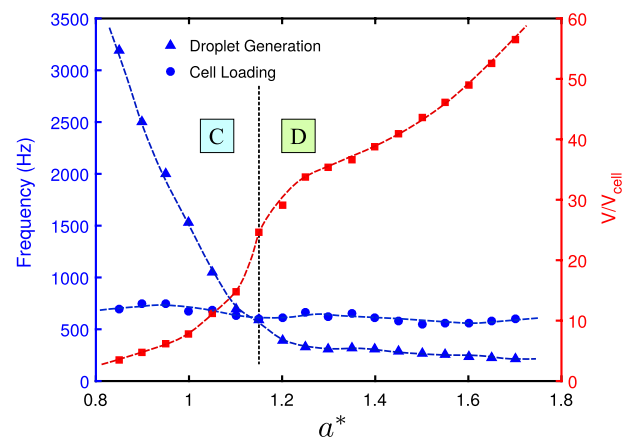


**Fig. 8** Frequency of compound droplet generation (triangles) versus frequency of cell loading (circles), and non-dimensional droplet size (squares) for configurations with different non-dimensional orifice radius at  $Ca_i = 10^{-3}$ ,  $Ca_o = 10^{-3}$  and  $\beta = 1$ . Different patterns are coded as C and D. Color patches represent different cell encapsulation modes: blue: Mode II, at most one cell per droplet; green: Mode III, at least one cell per droplet. (Color figure online)

droplet and the generated droplets are larger compared to the compound droplets in mode II. More interestingly, it is found that the pattern of droplet formation also changes above this critical  $a^*$ . For devices with small orifice radius, small uniform droplets form with relatively high frequency (C), while for relatively larger orifice radius, large droplets form with unpredictable uniformity (D).

## 5 Conclusion

A numerical study is carried out on cell encapsulation in a flow-focusing configuration using a three-phase front-tracking method. A phase diagram is developed for a range of



inner and outer capillary numbers, which classifies four different modes of successful or unsuccessful cell encapsulation for three viscosity ratios. The favorable mode of cell encapsulation predominantly occurs when  $\frac{Ca_i}{Ca_o} \simeq \mathcal{O}(1)$ . The cell encapsulation success rate decreases as  $Ca_i$  and  $Ca_o$  increase. By increasing the viscosity ratio, the modes of encapsulation shift toward higher  $Ca_i$  and lower  $Ca_o$ . For a fixed  $Ca_o = 10^{-3}$ , four different patterns of droplet formation are found for a combined non-dimensional parameter,  $Ca_\beta = Ca_i \times \beta^{-0.82}$ . The frequency profiles of droplet formation and cell loading reveal that each pattern has its own specific trend of droplet volume and frequency. A study of orifice radius effect on cell encapsulation shows a transition from mode II to mode III at  $a^* \simeq 1.15$ . The effect of orifice geometry on the encapsulation is also determined. For small orifice radius, the necking process helps with single-cell encapsulation for a wide range of inner and outer capillary numbers. It is also interesting that no multi-cell encapsulation was observed for the small orifice. As the orifice radius increases, keeping the other parameters fixed, the probability of cells loading the droplet increases, increasing the success rate of encapsulation. For all three orifice geometries studied, the favorable mode of cell encapsulation occurs for  $\frac{Ca_i}{Ca_o} \simeq \mathcal{O}(1)$ .

**Acknowledgements** The authors would like to acknowledge University of Central Florida Advanced Research Computing Center (Stokes Cluster) for providing required computational sources.

## Compliance with ethical standards

**Conflict of interest** The authors declare that they have no conflict of interest.

## References

- Abate AR, Chen CH, Agresti JJ, Weitz DA (2009) Beating Poisson encapsulation statistics using close-packed ordering. *Lab Chip* 9(18):2628
- Abate AR, Rotem A, Thiele J, Weitz DA (2011) Efficient encapsulation with plug-triggered drop formation. *Phys Rev E* 84(3):031502
- Akbari S, Pirbodaghi T (2014) Microfluidic encapsulation of cells in alginate particles via an improved internal gelation approach. *Microfluid Nanofluid* 16(4):773
- Anal AK, Singh H (2007) Recent advances in microencapsulation of probiotics for industrial applications and targeted delivery. *Trends Food Sci Technol* 18(5):240
- Anna SL, Bontoux N, Stone HA (2003) Formation of dispersions using flow focusing in microchannels. *Appl Phys Lett* 82(3):364
- Carrier O, Funfschilling D, Li HZ (2014) Effect of the fluid injection configuration on droplet size in a microfluidic T junction. *Phys Rev E* 89(1):013003
- Castillo-Orozco E, Kar A, Kumar R (2017) Electrospray mode transition of microdroplets with semiconductor nanoparticle suspension. *Sci Rep* 7(1):5144
- Che Z, Wong TN, Nguyen NT (2017) A simple method for the formation of water-in-oil-in-water (W/O/W) double emulsions. *Microfluid Nanofluid* 21(1):8
- Chen Y, Wu L, Zhang C (2013) Emulsion droplet formation in coflowing liquid streams. *Phys Rev E* 87(1):013002
- Chen Y, Wu L, Zhang L (2015) Dynamic behaviors of double emulsion formation in a flow-focusing device. *Int J Heat Mass Transf* 58:42
- Chong D, Liu X, Ma H, Huang G, Han YL, Cui X, Yan J, Xu F (2015) Advances in fabricating double-emulsion droplets and their biomedical applications. *Microfluid Nanofluid* 19(5):1071
- Chu LY, Utada AS, Shah RK, Kim JW, Weitz DA (2007) Controllable monodisperse multiple emulsions. *Angew Chem Int Ed* 46(47):8970
- Collins DJ, Alan T, Helmerson K, Neild A (2013) Surface acoustic waves for on-demand production of picoliter droplets and particle encapsulation. *Lab Chip* 13(16):3225
- Collins DJ, Neild A, Liu AQ, Ai Y (2015) The Poisson distribution and beyond: methods for microfluidic droplet production and single cell encapsulation. *Lab Chip* 15(17):3439
- Cruz-Mazo F, Montanero J, Gañán-Calvo A (2016) Monosized dripping mode of axisymmetric flow focusing. *Phys Rev E* 94(5):053122
- Derzsi L, Kasprzyk M, Plog JP, Garstecki P (2013) Flow focusing with viscoelastic liquids. *Phys Fluids* 25(9):092001
- Di Carlo D (2009) Inertial microfluidics. *Lab Chip* 9(21):3038
- Edd JF, Di Carlo D, Humphry KJ, Köster S, Irimia D, Weitz DA, Toner M (2008) Controlled encapsulation of single-cells into monodisperse picolitre drops. *Lab Chip* 8(8):1262
- Fornell A, Garofalo F, Nilsson J, Bruus H, Tenje M (2018) Intra-droplet acoustic particle focusing: simulations and experimental observations. *Microfluid Nanofluid* 22(7):75
- Glawdel T, Elbuku C, Ren CL (2012) Droplet formation in microfluidic T-junction generators operating in the transitional regime. II. Modeling. *Phys Rev E* 85(1):016323
- Gupta A, Sbragaglia M, Belardinelli D, Sugiyama K (2016) Lattice Boltzmann simulations of droplet formation in confined channels with thermocapillary flows. *Phys Rev E* 94(6):063302
- Haghshenas M, Wilson JA, Kumar R (2017) Algebraic coupled level set-volume of fluid method for surface tension dominant two-phase flows. *Int J Multiph Flow* 90:13
- Hirt CW, Nichols BD (1981) Volume of fluid (VOF) method for the dynamics of free boundaries. *J Comput Phys* 39(1):201
- Homma S, Moriguchi K, Kim T, Koga J (2014) Computations of compound droplet formation from a co-axial dual nozzle by a three-fluid front-tracking method. *J Chem Eng Jpn* 47(2):195
- Huebner A, Srisa-Art M, Holt D, Abell C, Hollfelder F, Edel JB (2007) Quantitative detection of protein expression in single cells using droplet microfluidics. *Chem Commun* 28(12):1218–1220
- Hunt NC, Grover LM (2010) Cell encapsulation using biopolymer gels for regenerative medicine. *Biotechnol Lett* 32(6):733
- Izbassarov D, Muradoglu M (2016) Effects of viscoelasticity on drop impact and spreading on a solid surface. *Phys Rev Fluids* 1(2):023302
- Lao KL, Wang JH, Lee GB (2009) A microfluidic platform for formation of double-emulsion droplets. *Microfluid Nanofluid* 7(5):709
- Liu H, Zhang Y (2009) Droplet formation in a T-shaped microfluidic junction. *J Appl Phys* 106(3):034906
- Liu W, Kim HJ, Lucchetta EM, Du W, Ismagilov RF (2009) Isolation, incubation, and parallel functional testing and identification by FISH of rare microbial single-copy cells from multi-species mixtures using the combination of chemistries and stochastic confinement. *Lab Chip* 9(15):2153
- Love JC, Ronan JL, Grotenbreg GM, van der Veen AG, Ploegh HL (2006) A microengraving method for rapid selection of single cells producing antigen-specific antibodies. *Nat Biotechnol* 24(6):703

- Migliarese C, Motta A, Tasoglu S, Gurkan UA, Guven S, Demirci U (2014) Organ printing and cell encapsulation. In: Scaffolds for tissue engineering: biological design, materials, and fabrication. Pan Stanford Publishing, pp 491–527
- Moon S, Ceyhan E, Gurkan UA, Demirci U (2011) Statistical modeling of single target cell encapsulation. *PLoS One* 6(7):e21580
- Murua A, Portero A, Orive G, Hernández RM, de Castro M, Pedraz JL (2008) Cell microencapsulation technology: towards clinical application. *J Controlled Release* 132(2):76
- Nabavi SA, Vladislavljević GT, Gu S, Ekanem EE (2015) Double emulsion production in glass capillary microfluidic device: parametric investigation of droplet generation behaviour. *Chem Eng Sci* 130:183
- Nie Z, Seo M, Xu S, Lewis PC, Mok M, Kumacheva E, Whitesides GM, Garstecki P, Stone HA (2008) Emulsification in a microfluidic flow-focusing device: effect of the viscosities of the liquids. *Microfluid Nanofluid* 5(5):585
- Nooranidoost M, Izbassarov D, Muradoglu M (2016) Droplet formation in a flow focusing configuration: effects of viscoelasticity. *Phys Fluids* 28(12):123102
- Nooranidoost M, Haghshenas M, Muradoglu M, Kumar R (2017) Cell-encapsulating droplet formation in a flow-focusing configuration. *Bull Am Phys Soc* 62:426–427
- Osher S, Sethian JA (1988) Fronts propagating with curvature-dependent speed: algorithms based on Hamilton–Jacobi formulations. *J Computat Phys* 79(1):12
- Seo M, Paquet C, Nie Z, Xu S, Kumacheva E (2007) Microfluidic consecutive flow-focusing droplet generators. *Soft Matter* 3(8):986
- Tan SH, Nguyen NT (2011) Generation and manipulation of monodispersed ferrofluid emulsions: the effect of a uniform magnetic field in flow-focusing and T-junction configurations. *Phys Rev E* 84(3):036317
- Tasoglu S, Kaynak G, Szeri AJ, Demirci U, Muradoglu M (2010) Impact of a compound droplet on a flat surface: a model for single cell epitaxy. *Phys Fluids* 22(8):082103
- Tryggvason G, Bunner B, Esmaeeli A, Juric D, Al-Rawahi N, Tauber W, Han J, Nas S, Jan YJ (2001) A front-tracking method for the computations of multiphase flow. *J Comput Phys* 169(2):708
- Unverdi SO, Tryggvason G (1992) A front-tracking method for viscous, incompressible, multi-fluid flows. *J Comput Phys* 100(1):25
- Utada A, Lorenceau E, Link D, Kaplan P, Stone H, Weitz D (2005) Monodisperse double emulsions generated from a microcapillary device. *Science* 308(5721):537
- Vladislavljević G, Kobayashi I, Nakajima M (2012) Production of uniform droplets using membrane, microchannel and microfluidic emulsification devices. *Microfluid Nanofluid* 13(1):151
- Wehking JD, Chew L, Kumar R (2013) Droplet deformation and manipulation in an electrified microfluidic channel. *Appl Phys Lett* 103(5):054101
- Wilson J, Wehking JD, Kumar R (2013) Uniform alumina microspheres from temperature induced forming in a microfluidic T-junction. *Appl Phys Lett* 103(20):203115
- Xu J, Li S, Tan J, Luo G (2008) Correlations of droplet formation in T-junction microfluidic devices: from squeezing to dripping. *Microfluid Nanofluid* 5(6):711
- Zhao CX (2013) Multiphase flow microfluidics for the production of single or multiple emulsions for drug delivery. *Adv Drug Deliv Rev* 65(11):1420
- Zhou C, Yue P, Feng JJ (2006) Formation of simple and compound drops in microfluidic devices. *Phys Fluids* 18(9):092105

**Publisher's Note** Springer Nature remains neutral with regard to jurisdictional claims in published maps and institutional affiliations.